On flow uniformity in various interconnects and its influence to cell performance of planar SOFC

C.M. Huang [a], S.S. Shy [a,*], C.H. Lee [b]

[a] *Department of Mechanical Engineering, National Central University, Jhong-li 32001, Taiwan*
[b] *Institute of Nuclear Energy Research, Lung-tan, Tao-yuan 32546, Taiwan*

ABSTRACT

This paper investigates flow uniformity in various interconnects and its influence to cell performance of a planar SOFC. A transparent hydraulic platform was used to measure flow uniformity in different rib-channel modules of interconnects. Several 3D numerical models implemented by CFD-RC packages were established to first simulate these hydraulic experiments and then used to evaluate the cell performance of a single-cell stack using different designs of interconnects with different flow uniformity over a wide range of a hydraulic Reynolds number (Re) based on a hydraulic diameter of rib-channels. Numerical flow data are found in good agreement with experimental results. It is proposed that a new design, using simple small guide vanes equally spaced around the feed header of the double-inlet/single-outlet module, can effectively improve the degree of flow uniformity in interconnects resulting in 11% increase of the peak power density (PPD) which can be further increased when applying a Ni-mesh on anode. Numerical analyses demonstrate a strong influence of Re on cell performance, of which appropriate ranges of Re in both anode and cathode sides are identified for achieving a reasonably good PPD while remaining an economic fuel utilization rate and having less temperature variations in the single-cell stack.

© 2008 Elsevier B.V. All rights reserved.

1. Introduction

The planar solid oxide fuel cell (SOFC), a high-temperature clean energy device, has been recently recognized as a promising candidate for the future medium-sized electricity power generation industry (1–10 MW) [1]. However, real SOFC stack designs are complex. Many challenges, such as mass and heat transports together with electrochemical reactions, optimization of geometry and development of new materials, still remain to be solved step by step with limited but controllable parameters before the status of the development can be elevated from a module level. One facet of the problem is the geometric design of planar interconnects (bipolar plates) which act as gas distributors to separate and provide uniform flow fields in both anode (fuel) and cathode (oxidant) while providing the necessary support and making the electrical connection among cells. The optimal design of interconnects requires a uniform distribution of fuel on the anode to achieve a homogeneous diffusion process into the electrode and a uniform airflow on the cathode to remove heat during long-term cell operation [2,3]. To the authors' best knowledge, yet no experimental data are available to evaluate the degree of flow uniformity among different designs of

interconnects and its influence to the cell performance of planar SOFCs. This motivates the present work.

A typical flow pathway of interconnects in a planar SOFC includes three parts, starting from the feed header to multi-flow channels usually divided by many rectangular ribs to the exhaust header. Two commonly used flow distributors of interconnects deserve to comment, a module proposed by Yakabe et al. [4] with a single-inlet/single-outlet design having many parallel rectangular channels in the middle (Fig. 1a) and a module adopted by de Haart et al. [5] with a double-inlet/single-outlet design having similar parallel rectangular flow channels (Fig. 1b). These two flow distributors have been applied in many numerical simulations of cell performance relative to different flow arrangements (e.g., co-flow, counter-flow and cross-flow at an angle of 90°). Under the assumption of uniform flow velocity distributions in interconnects, Lin et al. [6] studied analytically the effect of rectangular ribs on the concentration polarization. Similarly, Li et al. [7] investigated numerically the shape of cylindrical ribs in attempt to increase the reactant contact area with the electrode/electrolyte surface. Furthermore, quite a few researchers have also made an attempt to study complex thermo-fluid electrochemical transport phenomena in planar SOFCs with various fuel cell boundary and interfacial conditions, such as the combined thermal boundary conditions on solid walls, mass transfer associated with the electrochemical reaction and gas permeation across the interface, see Refs. [2–4,6–10] among others.

Nomenclature

D_h	hydraulic diameter (m)
E	potential gradient ($V\,m^{-1}$)
h	height (m)
h_0	enthalpy ($J\,kg^{-1}$)
i	charge flux ($A\,m^{-2}$)
J	mass diffusion flux ($kg\,m^{-2}\,s^{-1}$)
j_C	current density ($A\,m^{-3}$)
K_E	electrical conductivity ($\Omega^{-1}\,m^{-1}$)
n	total number of rib-channels
p	pressure (Pa)
q	heat flux ($J\,m^{-2}\,s^{-1}$)
r	reaction rate ($kmol\,m^{-3}$)
Re	Reynolds number
T	temperature (K)
u_i	mean velocity ($m\,s^{-1}$)
$\bar{u}$	averaged mean velocity ($m\,s^{-1}$)
$\vec{U}$	velocity vector ($m\,s^{-1}$)
Y	species mass fraction
w	width (m)

Greek letters

Γ	index of flow uniformity
ε	porosity
η	overvoltage (V)
κ	permeability (m^{-2})
λ	thermal diffusivity ($J\,m^{-1}\,K^{-1}$)
μ	dynamic viscosity ($kg\,m^{-1}\,s^{-1}$)
ν	kinematic viscosity ($m^2\,s^{-1}$)
ρ	density ($kg\,m^{-3}$)
σ	electrical conductivity ($S\,m^{-1}$)
τ	stress tensor ($N\,m^{-2}$)
$\dot{\omega}$	production rates ($kg\,m^{-3}\,s$)

Subscripts

F	ionic phase
i	Arabic number of rib-channels
j	species
S	solid phase

It should be noted that all of these aforementioned studies on flow uniformity in interconnects for planar SOFCs were either numerical simulations or mathematical models. Hence, there is a need to devise an idealized experimental platform that allows direct imaging and velocity measurements of flow distributions in rib-channels of interconnects in order to test the accuracy of numerical flow data. This is our first objective.

The second, but equally important, objective is to investigate the effect of flow uniformity on the cell performance of a single-cell stack via three-dimensional numerical models based on CFD-RC packages with sub-models for various transport phenomena and electrochemical reactions. Recent numerical simulations [8,9] proposed that the counter-flow configuration has a higher peak power density than co-flow and cross-flow configurations, but it may suffer a more non-uniform temperature distribution across the positive electrode–electrolyte-negative electrode (PEN). The latter may affect the longevity of the cell through its influence on thermal stresses among cell components and need further improvement. Thus, this study uses the counter-flow configuration to evaluate for the first time the degree of flow uniformity in various designs of interconnects and its influence on the cell performance.

For clarity, the experimental and numerical approaches for non-reacting and reacting flows are sequentially described in the following sections. It will be showed in due course that a new design using small guide vanes in the feed header of interconnects can uniformly distribute flows through rib-channels and thus the degree of flow uniformity can be effectively improved. Then the numerical results will be presented revealing the influence of flow uniformity and the effect of a hydraulic Reynolds number (Re) based on a hydraulic diameter of flow rib-channels on the cell performance of the single-cell stack. Furthermore, the use of a Ni-mesh on the anode, as that proposed recently by Teller et al. [11], for the enhancement of cell performance is simulated and discussed. Finally, appropriate ranges of Re in both anode and cathode sides are identified in order to achieve a reasonably good power density while remaining a more economic fuel utilization rate and having a less temperature variation in the single-cell stack.

2. Experimental

Fig. 2a presents schematic diagrams of a transparent gravity-driven hydraulic platform, mainly consisting of a large water tank and a small dye tank with a pair of dye–fluid supply tubes having an adjustable width. This hydraulic platform, designed for visualizing the full flow fields inside various rib-channel designs of interconnects and thus measuring the degree of flow uniformity in various interconnects, was recently presented in SOFC-X [12]. For completeness, a brief description is included. Both water and dye tanks have a constant level of a fixed internal volume, so that the volume flux controlled by flow meters can be kept constant during a run. Many different modules of interconnects, including various designs of rib-channels for both cathode and anode, are tested for their flow uniformity. All modules of interconnects are transparent,
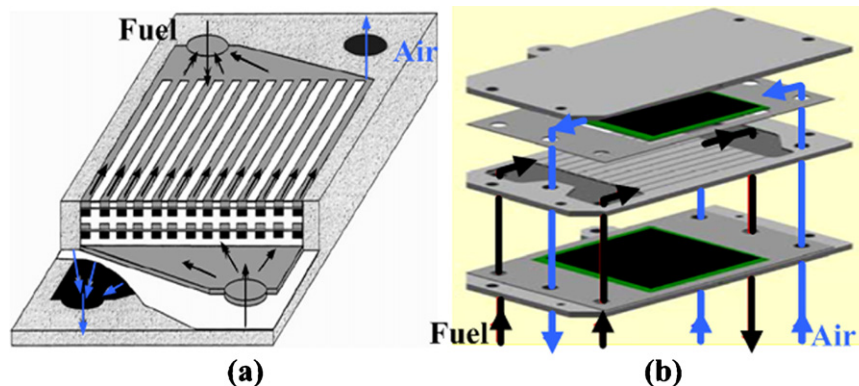

Fig. 1. (a) The single-inlet/single-outlet design of interconnects proposed by Yakabe et al. [4]. (b) The double–inlet/single-outlet design used by de Haart et al. [5].
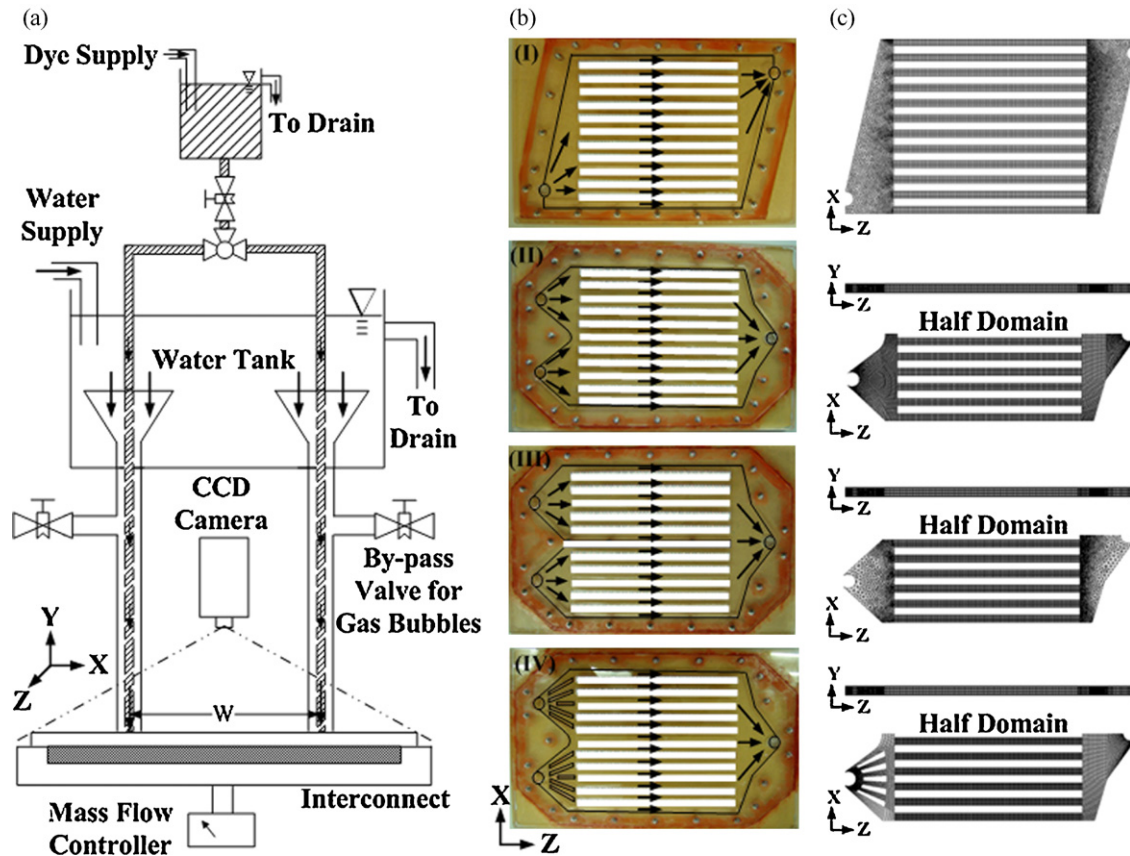
Fig. 2. (a) Schematic diagrams of the hydraulic platform for flow visualizations and velocity measurements in interconnects. (b) Four different designs of rib-channels modules for interconnects. (c) The corresponding four numerical flow models, where only half domains are simulated for designs II, III and IV due to the symmetry.

made of Plexiglas for direct flow visualizations and velocity measurements. For simplicity, this paper only presents four different designs using the same 12 rectangular flow channels divided by eleven ribs (Fig. 2b), respectively, (I) the single-inlet/single-outlet design [4], (II) the double-inlet/single-outlet design [5], (III) same as (II) but with an extended rib in the center dividing symmetrically these 12 flow channels into two portions, and (IV) same as (II) but with 10 small guide vanes equally spaced in the feeder region. All modules are horizontally positioned on the bottom of the hydraulic platform, and their feeders (inlets) are connected to the dye–fluid supply tubes for testing the degree of flow uniformity in these rib-channels for each of four different designs.

The hydraulic Reynolds number, $Re = \bar{u}D_h/\nu$, is defined and used to control flow rates for these different modules, where $\bar{u}$ is the averaged mean velocity from 12 rib-channels, ν is the kinematic viscosity of the fluid, and $D_h = 2wh/(w+h)$ is the hydraulic diameter. Note that w and h are the width and the height of rib-channels. Various sizes of interconnects ranging from 5 cm × 5 cm to about 30 cm × 30 cm for the total area of 12 rib-channels are tested, in which the dynamic similarity of these flows is found provided that values of Re are not too high and the flows remain laminar. For steady, laminar, incompressible flows without the consideration of mixing, just as in the present flow, flow behaviors using either water or gas as the working fluid are essentially similar. Thus, the flow uniformity results obtained in the water experiment are useful in understanding flow distributions in real SOFC at least in a qualitative sense. Nevertheless, the main purpose of such water experiment is to test the accuracy of flow numerical models using water as the working fluid. Hence, the validated flow models can be then established to simulate gaseous transport phenomena and electrochemical reactions in a single-cell stack.

This study measures the effect of Re on flow uniformity in these aforementioned four different modules. Though the value of Re can be varied from 0 to a few thousands in the present setup, our focus is within the range of $0 < Re < 350$ which are comparable to that used in real testing and operation conditions [13]. A high-speed CCD camera with variable frame rates from 30 to 1000 frames s^{-1} is applied to record the time evolution of the dye–fluid flowing through these 12 rib-channels of various modules. The obtained dye-flow images are then binarized to extract corresponding advanced displacements as a function of time in each of these 12 rib-channels for all different modules and thus the averaged mean velocities can be measured, as to be discussed.

3. Numerical simulation

Several 3D numerical models under the assumption of steady, laminar, and incompressible flows for both non-reacting and reacting cases were established using CFD-RC package with sub-models. For the non-reacting case, the aforementioned hydraulic experiments including four different designs were simulated, as shown on Fig. 2c. Due to the symmetry, for designs II, III and IV, only one half of the flow fields were simulated. It will be demonstrated in due course that numerical flow velocity data are in good agreement with experimental results and the design IV using small guide vanes has the highest degree of flow uniformity among four different modules (Fig. 2). For simplicity, this paper considers the designs II and IV in the reacting case (Fig. 3a and b), so that different degrees of flow uniformity on the cell performance of the same single-cell stack can be investigated. Moreover, Fig. 3c presents a cross-sectional structure of the single-cell stack, where a Ni-mesh of 0.8 mm in thickness is optionally applied on the anode for the
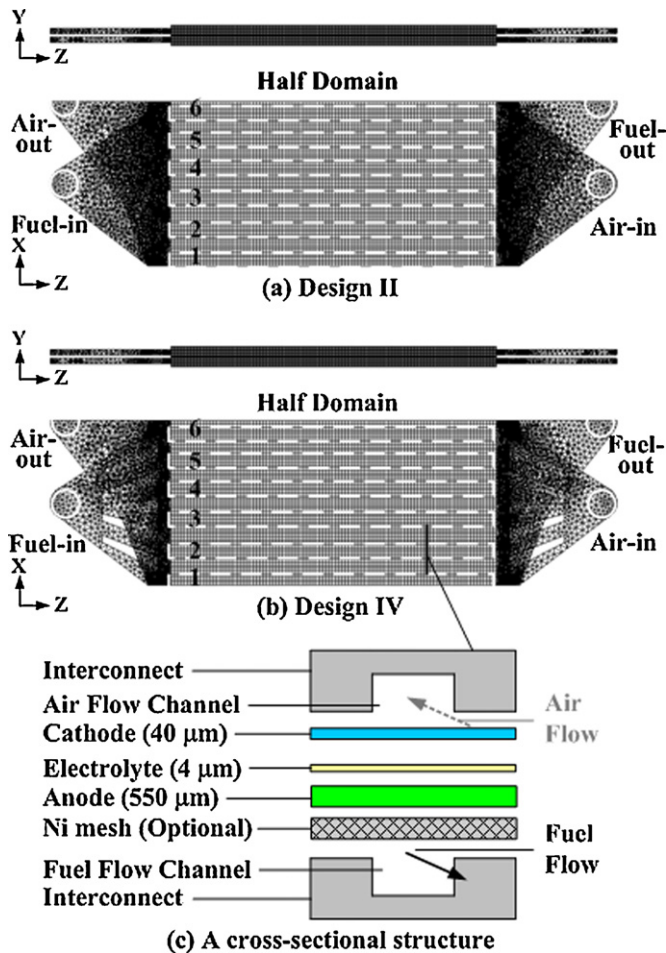
Fig. 3. Two reacting flow models for a single-cell stack using different designs of interconnects: (a) without guide vanes and (b) with guide vanes, where the Arabic numbers (1–6) indicate six rib-channels in the half domain of the cell. (c) A cross-sectional structure of the single-cell stack.

Table 1
A list of governing equations used

Mass	$\nabla(\varepsilon\rho\overline{U}) = 0$
Momentum	$\nabla(\varepsilon\rho\overline{U}\,\overline{U}) = -\varepsilon\nabla p + \nabla(\varepsilon\tau) + \frac{\varepsilon^2\mu\overline{U}}{\kappa}$
Concentration	$\nabla(\varepsilon\rho\overline{U}Y_j) = \nabla J_j + \dot{\omega}_j$
Energy	$\nabla(\varepsilon\rho\overline{U}h_0) = \nabla q + \varepsilon\tau\nabla\overline{U} + j_C\eta + \sigma E^2$ $q = \lambda\nabla T + \sum J_j h_j$
Charge	$\nabla i_S = -\nabla i_F$

design IV to estimate the further increase of the power density due to the use of Ni-mesh. Even though efforts were made to test the grid sensitivities and to reduce the CPU time while remaining the data accuracy, these reacting models all contained more than 300,000 grid numbers and thus very time-consuming to perform the simulations.

Using CFD-RC, the cell-centered control volume approach was employed to integrate the mass, momentum, concentration, heat

and charge fluxes across the faces of the control volume in all three directions, and the SIMPLEC algorithm was used to implement the velocity–pressure coupling on a staggered grid arrangement [14]. The associated governing equations written in vector and tensor forms are listed in Table 1, where the conservation equations of mass and momentum are used in both the header and flow rib-channels to simulate the full flow field in interconnects. The Darcy's law was employed in porous electrodes and/or Ni-mesh. Several sub-models, for instances ideal gas law for the mixtures of species, the Stefan–Maxwell equation for the mass transfer of gaseous molecules, and the Bulter–Volmer equations for the correlation between electrochemical reactions and current density, were also applied to simulate transport phenomena and electrochemical reactions in the single-cell stack.

The present simulation neglects the gravity with the assumptions that the hydraulic and electrical resistances as well as porous media are isotropic and homogeneous, where constant gas diffusion coefficient and thermal and electrical conductivities are also assumed. Table 2 lists the relevant physical properties of the PEN, including the thickness, porosity, permeability, thermal and electrical conductivities. Fuels are syngases with compositions of 9.6% H_2, 26% CO, 21.6% CO_2, and 42.8% H_2O based on the mass fraction and the oxidant air having 79% N_2 and 21% O_2. Since hydrogen can be reformed from carbon monoxide at high-temperature conditions, the water-gas-shift reaction, $CO + H_2O \leftrightarrow CO_2 + H_2$, in both fuel channels and porous anode having a reaction rate described by the Arrhenius law [15–17] as below:
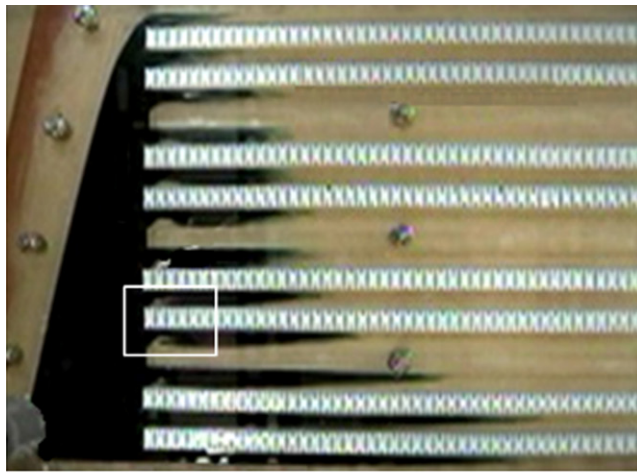
$$r = 1199T^2 \exp\left(\frac{-12509}{T}\right)[CO][H_2O]$$
$$- 6.77 \times 10^4 T^2 \exp\left(\frac{-16909}{T}\right)[CO_2][H_2]$$

is also considered. The parentheses [ ] represent the concentration of species in units of kmol m^{-3}. For the reaction on the anode, hydrogen is oxidized via $H_2 + O^{2-} \rightarrow H_2O + 2e^-$. Simultaneously, the reduction of oxidant occurs at the cathode is via $1/2\,O_2 + 2e^- \rightarrow O^{2-}$. The electrochemical reaction of CO is neglected because its oxidation rate is much slower than that of H_2 [18]. Finally, the exchange current densities used in the Butler–Volmer equations for both anode and cathode are set as 10^{13} and 10^{12} A m^{-3}, respectively.
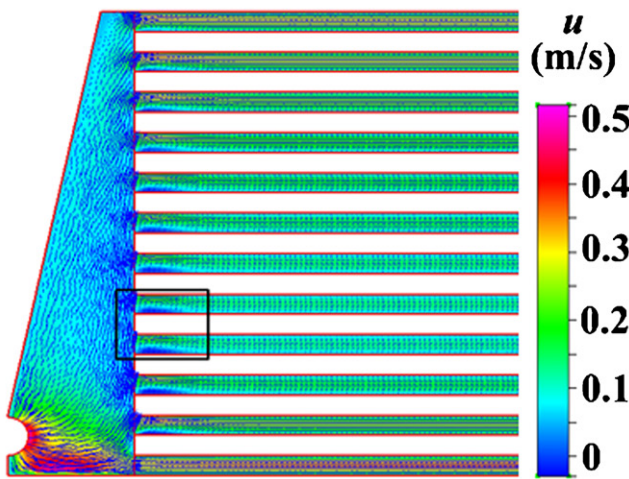
4. Results and discussion
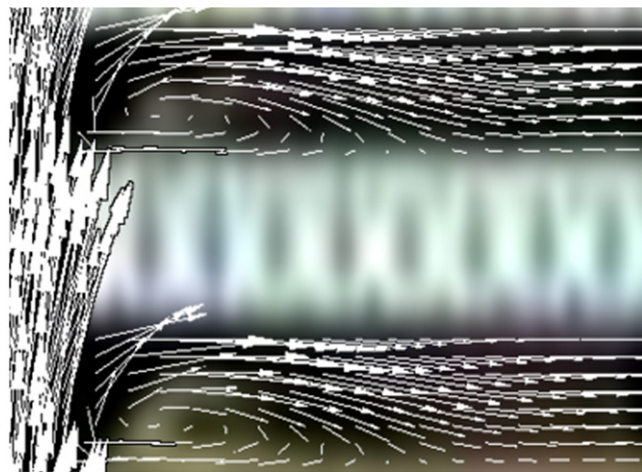
4.1. Flow recirculation zones in interconnects

The beauty of the design I proposed by Yakabe et al. [4] was its simplicity containing only one inlet/one outlet, but it may induce some flow recirculation zones in rib-channels. Fig. 4 shows typical flow recirculation zones occurred near the entrance of rib-channels for the single-inlet/single-outlet module (design I), including (a) an instantaneous experimental flow image, (b) the corresponding numerical velocity data, and (c) data of a small rectangular region as marked on Fig. 4a and b where both dye-flow image and numerical velocity vectors are superimposed to clearly show these recirculation zones. As can be seen, the existence of these recirculation zones in the design I can make local velocity distributions highly non-uniform which in turn may result in large non-uniform

Table 2
The PEN properties for simulations

Component	Thickness (μm)	Porosity (%)	Permeability (m^2)	Thermal conductivity (W m^{-1} K^{-1})	Electrical conductivity (1 Ω^{-1} m^{-1})
Cathode	40	50	10^{-12}	9.6	7700
Electrolyte	4	1	10^{-18}	2.7	10^{-20}
Anode	550	40	10^{-12}	6.23	10^5

(a)

(b)

(c)

Fig. 4. (a) An instantaneous flow image of the design I showing flow recirculation zones in the entrance regions of rib-channels; (b) the corresponding numerical flow simulation results. (c) Same as (a) and (b), but plotted only for a small region marked by the rectangular window in (a) and (b) where both dye-flow image and numerical flow velocity data are superimposed to demonstrate flow recirculation zones.
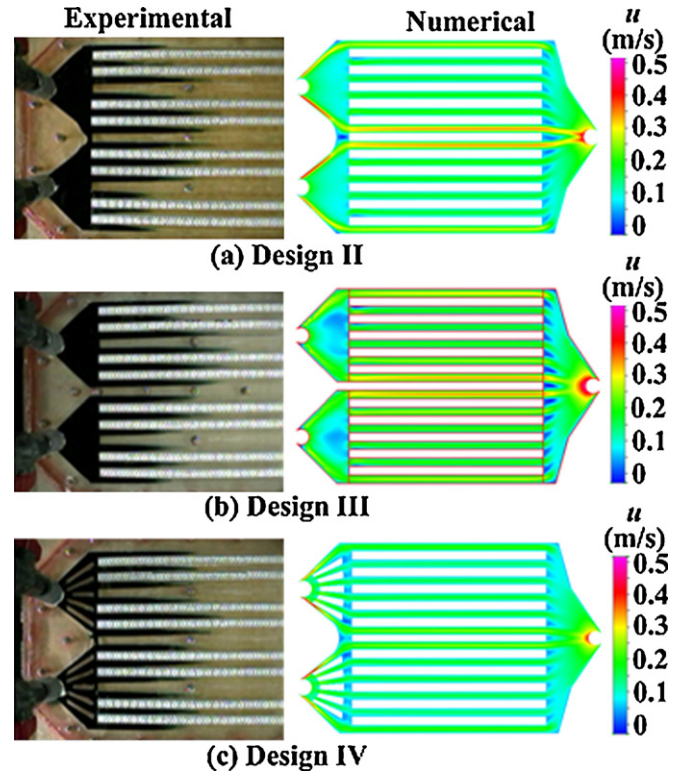

(a) Design II

(b) Design III

(c) Design IV

Fig. 5. Instantaneous dye-flow images (left) and corresponding numerical velocity distributions (right) for designs II, III, and IV, respectively.

temperature gradients locally making the cell more vulnerable to the unwanted concentration polarization. Such flow recirculation zones in the design I are found for all values of Re studied.

4.2. Velocity distributions and flow uniformity in interconnects

As typical examples, both experimental and numerical flow data for designs II, III and IV are presented on Fig. 5a–c, respectively. The time evolutions of these dye fronts flowing through 12 rib-channels for each of four different designs of interconnects (Figs. 4 and 5) were recorded to obtain the advanced displacement of these dye fronts as a function of time in each of twelve rib-channels, as shown on Fig. 6. These displacement–time data on Fig. 6 all demonstrate linear increase satisfying the steady condition and thus their slopes can be used to represent the mean velocities in rib-channels. Fig. 7 presents experimental velocity data in these 12 rib-channels for four different designs together with numerical velocity data marked by gray bars for comparison. Note that these velocity data are normalized by the corresponding averaged mean velocities ($\bar{u}$) which are obtained by averaging 12 mean velocities in rib-channels for each of four different modules. Numerical velocity data are found in very good agreement with experimental data. As can be seen from Figs. 6 and 7, the design IV has the smallest variation of velocity distributions among all different modules of interconnects studied. By using 10 guide vanes equally spaced around the feeder region, both experimental and numerical results show that the flow uniformity can be effectively increased and flow recirculation zones near the entrance of rib-channels can be eliminated. This flow uniformity improvement is valid for all different sizes of interconnects studied ranging from 5 cm × 5 cm to 30 cm × 30 cm which are the total area of rib-channels.
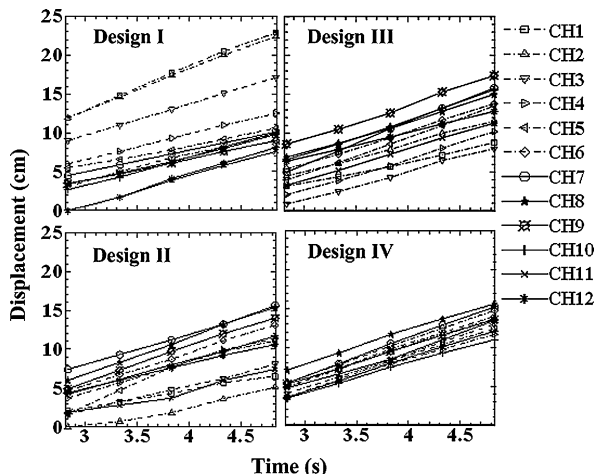
Fig. 6. Time evolutions of the advanced displacements of dyed fluid fronts in these 12 flow channels (CH1–CH12) for four different designs, where the flow Reynolds number is fixed at a constant of $Re = 170$.

For quantitative estimation, an index of flow uniformity is defined as below:

$$\Gamma = 1 - \left\{ \frac{1}{n} \sum_{i=1}^{n} \left[\frac{(u_i - \bar{u})}{\bar{u}} \right]^2 \right\}^{1/2},$$

where $n = 12$ represents the total number of rectangular rib-channels for each of four different designs, u_i is the velocity at ith rib-channel, and $\bar{u}$ is the averaged mean velocity, respectively. The result is presented on Fig. 8, showing the degree of flow uniformity at various values of Re for four different designs of interconnects. As can be seen, the flow uniformity of the design I (Yakabe et al. [4]) is slightly better than the design II (de Haart et al. [5]) but the former has a more sever recirculation problem in the entrance region of rib-channels as discussed previously. It is found that the design
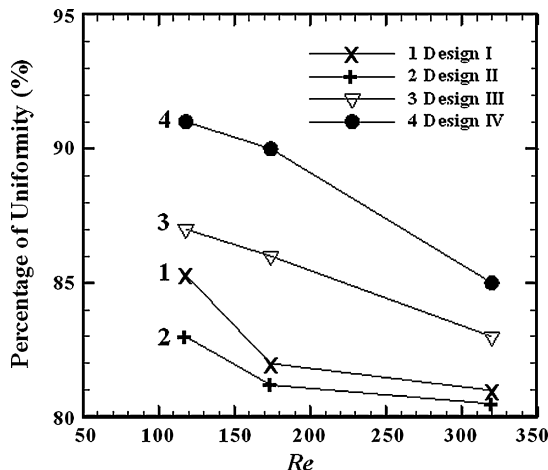

Fig. 7. Comparisons of experimental and numerical velocity distributions in these twelve flow channels for four different designs, where $\bar{u}$ is the mean velocity averaged from these data in 12 channels.

Fig. 8. The degree of flow uniformity plotted against Re for four different designs of interconnects using the same rib-channels.

IV using simple small guide vanes, equally spaced around the feed header of the double-inlet module, features a highest degree of flow uniformity among all different modules studied, where $\Gamma = 91\%$ compared to $\Gamma = 83\%$ for the design II at the same $Re = 120$. As values of Re increase, the degree of flow uniformity decreases for all different designs, suggesting that Re plays a role on flow uniformity in interconnects, as to be discussed in detail later.

4.3. Effect of flow uniformity on cell performance

Numerical simulations on the cell performance of the single-cell stack (Fig. 3) were performed in two different designs of interconnects (designs II and IV) having different degrees of flow uniformity. Fig. 9a and b shows the effect of flow uniformity on temperature variations of the PEN with a surface area of $25\,\text{mm} \times 50\,\text{mm}$ (half domain due to symmetry) for designs II and IV, where the experimental conditions were kept the same with $Re_{\text{fuel}} = 20$ and $Re_{\text{air}} = 300$ for both cases. As can be seen, values of temperature on the PEN tend to decrease gradually from 1125 to 1090 K along the z-direction, as indicated by color bars as well as constant temperature contour lines. Such temperature variations on the PEN are due to the counter-flow geometry applied and the higher value of $Re_{\text{air}} = 300$ on the cathode side. When comparing the results between Fig. 9a and b, it is found that flow uniformity plays a role on the temperature distribution of the PEN, for which some local hot spots (the maximum temperature of 1125 K) near the first three rib-channels in the design II can be observed while no local hot spots in the design IV. This is because the latter applies simple guide vanes in the header of interconnects that can increase flow uniformity making a more uniform electrochemical reaction on the PEN and thus resulting in a more uniform temperature distribution of the PEN (Fig. 9b). It should be noted that the "wiggling" patterns of constant temperature contour lines on the PEN in the x-direction, as shown on Fig. 9a and b, are due to the geometric structures of rib-channels, in which the PEN on the area of flow channels is more active than that just on the ribs. Such temperature non-uniformity in the x-direction can be significantly reduced by using a layer of Ni-mesh as a contact layer on the anode, please see both Figs. 3c and 9c. Thus, a balance use of the catalyst in the anode can be achieved, which in turn greatly improves the temperature uniformity of the PEN in the x-direction. This result demonstrates the advantage of using the Ni-mesh on the anode supporting a previous study by Teller et al. [11].
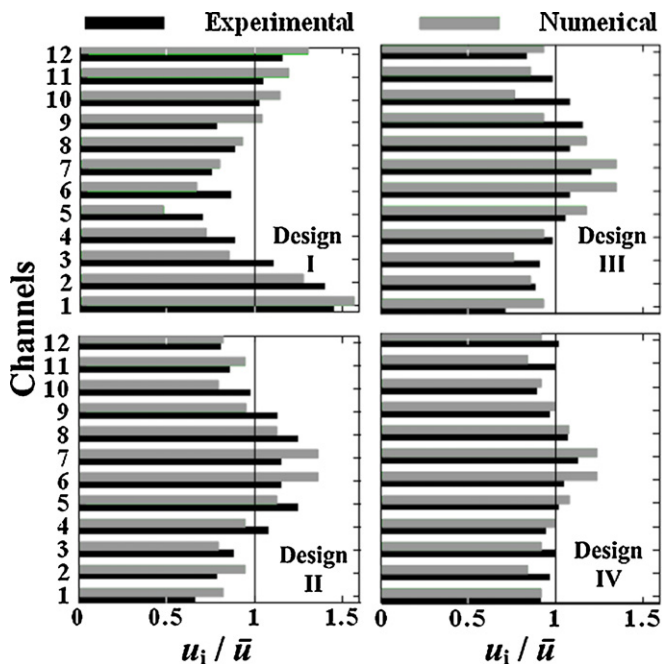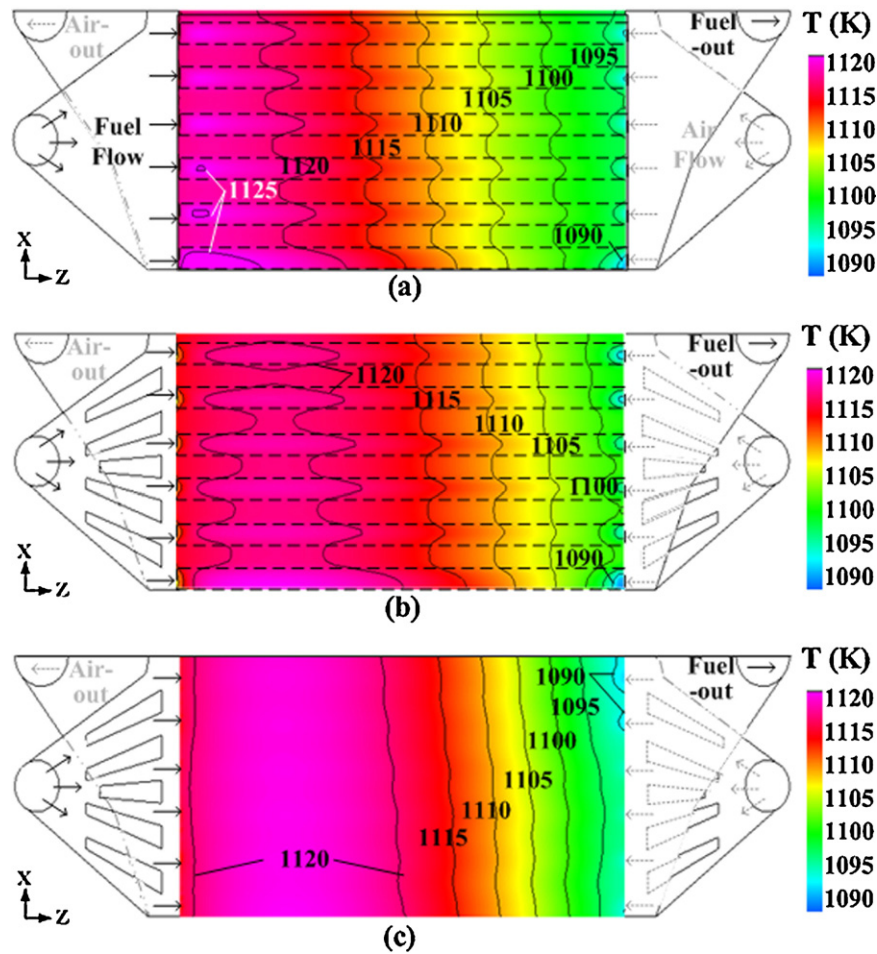
Fig. 9. Temperature distributions on the anode surface for (a) design II, (b) design IV, and (c) design IV with an additional Ni-mesh by holding $Re_{fuel} = 20$ and $Re_{air} = 300$ fixed in the same single-cell stack.

Same conditions as Fig. 9, Fig. 10 shows the corresponding voltage and power density as a function of current density for three different cases using the same single-cell stack with fixed $Re_{fuel} = 20$ and $Re_{air} = 300$, so that the cell performance at different degrees of
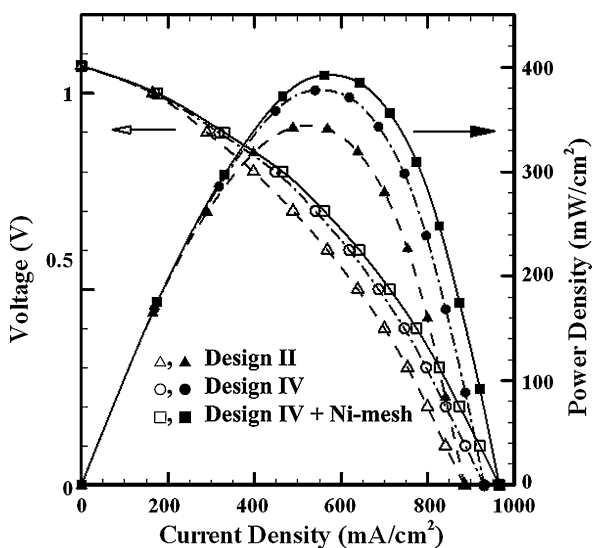

Fig. 10. Same conditions as Fig. 9, but plotted for comparisons of current–voltage and current–power density variations in three different cases.

flow uniformity can be scrutinized. The ohmic loss at low current is influenced by the electrical conductivity (K_E) of interconnects and/or electrodes. At fixed thicknesses of the interconnects and the electrodes, the higher the K_E is, the smaller the ohmic loss is. According to the study of the Pacific Northwest National Laboratory (PNNL), values of K_E for commonly used alloy interconnects can be varied from $7.6 \times 10^5 \ \Omega^{-1} \, m^{-1}$ (Ni–Cr–Fe-based alloy, Haynes R-41) to $5.9 \times 10^7 \ \Omega^{-1} \, m^{-1}$ (Ferritic stainless steels, Kanthal silver FCC) [19]. Since this study focuses on how to enhance the cell performance by improving the degree of flow uniformity in interconnects, a higher electrical conductivity of interconnects ($K_E = 10^7 \ \Omega^{-1} \, m^{-1}$) is assumed, resulting in a tiny ohmic loss on Fig. 10. It is found that the value of peak power density (PPD $\approx$ 380 mW cm^{-2}) occurring near 550 mA cm^{-2} for the design IV using small guide vanes is 11.1% higher than the design II (PPD = 342 mW cm^{-2}). Clearly, this increase in the value of PPD points to the important influence of flow uniformity in interconnects on the cell performance. By using simple guide vanes in the feed header region of interconnects, the degree of flow uniformity in interconnects can be effectively increased which in turn reduce unwanted temperature variations, help to maintain uniform electrochemical performance of electrodes via the mass transport normal to their surface, and thus increase the power density of the cell. When applying the Ni-mesh to the design IV, the value of PPD can be further increased to 392 mW cm^{-2} which is 14.6% higher than that of the design II. The Ni-mesh serves as a contact layer which can significantly eliminate the "wiggling" temperature variations across the ribs and their
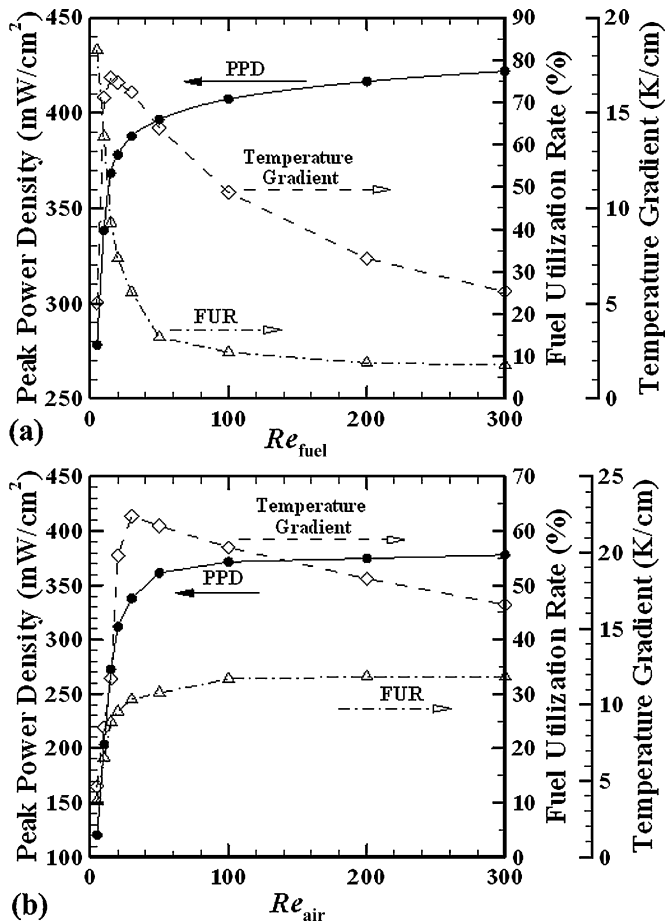
Fig. 11. Effects of Re_{fuel} and Re_{air} on the cell performance while keeping (a) Re_{air} = 300 and (b) Re_{fuel} = 20 fixed.

adjacent flow channels (Fig. 9) and thus achieve a higher value of PPD due to a balance use of the catalyst on the anode.

4.4. Effects of Re_{fuel} and Re_{air} on cell performance

Numerical analyses on the effect of Re_{fuel} (anode) to the fuel utilization rate, FUR $\equiv [1 - (\text{fuel}_{out}/\text{fuel}_{in})] \times 100\%$, and the PPD of the single-cell stack as discussed using the design IV (Fig. 3b) are performed over a wide range of Re_{fuel} varying from about 5 to 300 while keeping Re_{air} = 300 fixed. The result is presented on Fig. 11a. It is found that the PPD value first increases drastically from 278 to 396 mW cm^{-2} when Re_{fuel} increases from 5 to 50 and then quickly levels off having a gradual increase with Re_{fuel} up to 425 mW cm^{-2} when Re_{fuel} = 300. This result indicates that Re_{fuel} has a strong influence on the PPD especially when Re_{fuel} < 50. It is worthy noting that the actual amount of fuel consumed for electrochemical reactions increases with Re_{fuel} just like the profile of PPD on Fig. 11a. Hence, the decrease profile of FUR with Re_{fuel} shows an opposite trend with the profile of PPD. The value of FUR decreases significantly from about 82% to about 15%, when the value of Re_{fuel} increases from 5 to 50. Further increasing Re_{fuel} up to 300, the value of FUR decreases gradually to about 8%. Only a certain amount of fuel supplied can allow penetrating through the porous medium, because the Darcy's drag force imposed by the pore walls can exert resistances on the fluid usually resulting in a pressure drop across the porous medium. This should be responsible for causing the present decreasing profile of FUR. Also plotted on Fig. 11a is the variation of the temperature gradient on the anode surface with Re_{fuel},

where the maximum temperature gradient (16.5 Kcm^{-1}) occurs at Re_{fuel} = 15. At higher values of Re_{fuel}, the excess fuel can help to reduce the temperature gradient on the surface of the anode.

Fig. 11b has the same format as Fig. 11a but for the effect of Re_{air} on the cell performance, where values of Re_{air} are varied from 5 to 300 by holding Re_{fuel} = 20 fixed. The profiles of PPD and temperature gradient are found to be very similar to that of Fig. 11a. Since the fuel mass flow rate is fixed because of constant Re_{fuel} = 20, the profile of FUR increases with Re_{air} on the same trend as the PPD profile. Both values of FUR and PPD reach their maximum values and are independent of Re_{air} when $Re_{air} \geq 100$. For Re_{fuel} = 20, much larger values of Re_{air} ($\gg 20$) are required to consume the fuel for electrochemical reactions, because the reduction rate of oxygen on the cathode is much slower than the oxidation rate of hydrogen on the anode. It is seen on Fig. 11b that increasing Re_{air} is useful for the effective heat removal and thus reduces the temperature gradient on the anode surface. However, too high values of Re_{air} are not practical, because the flow may become turbulent. Based on these aforementioned results, it is proposed that values of Re_{fuel} and Re_{air} should be operated at a range from 20 to 50 on the anode and from 200 to 300 on the cathode in order to achieve a reasonably good power density while remaining an economic fuel utilization rate and having an effective heat removal.

5. Conclusions

This study measures the degree of flow uniformity in many different rib-channel modules of interconnects and its influence to the cell performance of a planar SOFC. These experimental and numerical simulations reveal the following points:

(1) It is found that a new design using small guide vanes equally spaced around the feed header of the double-inlet/single-outlet module of rib-channel interconnects features a highest degree of flow uniformity among all different modules studied. This improvement on flow uniformity in interconnects can effectively remove local hot spots on the PEN and increase the peak power density of the single-cell stack at least up to 11%.
(2) Furthermore, when applying a Ni-mesh as the contact layer on the anode, a balance use of the anode's catalyst can be obtained, the "wiggling" temperature variations across the ribs and their adjacent flow channels can be significantly eliminated, and the power density of the cell can be further increased.
(3) Numerical results demonstrate a strong influence of Re_{fuel} and Re_{air} on the cell performance. At a given value of Re_{fuel}, much larger values of Re_{air} are required to consume completely the available fuel for electrochemical reactions, because the reduction rate of oxygen on the cathode is much slower than the oxidation rate of hydrogen on the anode. It is suggested that values of Re_{fuel} and Re_{air} should be operated at a range from 20 to 50 on the anode and from 200 to 300 on the cathode for achieving a reasonably good power density while remaining an economic fuel utilization rate and having a smaller temperature gradient based on simulations of the cell performance in the single-cell stack.

These results should be useful for further improvement of the cell performance of planar SOFCs.

Acknowledgments

References

[1] S.C. Singhal, K. Kendall, High Temperature Solid Oxide Fuel Cells: Fundamentals, Design and Applications, Elsevier, Kidlington, 2003, pp. 363–364.
[2] T. Ackmann, L.G.J. de Haart, W. Lehnert, D. Stolten, J. Electrochem. Soc. 150 (2003) A783–A789.
[3] N. Autissier, D. Larrain, J. Van herle, D. Favrat, J. Power Sources 131 (2004) 313–319.
[4] H. Yakabe, T. Ogiwara, M. Hishinuma, I. Yasuda, J. Power Sources 102 (2001) 144–154.
[5] L.G.J. de Haart, I.C. Vinke, A. Janke, H. Ringel, F. Tietz, in: H. Yokpawa, S.C. Singhal (Eds.), Solid Oxide Fuel Cells (SOFC VII), The Electrochemical Society Proceedings Series, Pennington, New Jersey, 2001, PV2001-16, p. 111.
[6] Z. Lin, J.W. Stevenson, M.A. Khaleel, J. Power Sources 117 (2003) 92–97.
[7] P.W. Li, S.P. Chen, M.K. Chyu, J. Power Sources 140 (2005) 311–318.
[8] K.P. Recknagle, R.E. Williford, L.A. Chick, D.R. Rector, M.A. Khaleel, J. Power Sources 113 (2003) 109–114.
[9] Y.P. Chyou, T.D. Chung, J.S. Chan, R.F. Shie, J. Power Sources 139 (2005) 126–140.
[10] S.B. Beale, J. Power Sources 128 (2004) 185–192.
[11] O. Teller, W.A. Meulenbert, F. Tietz, E. Wessel, W.J. Quadakkers, in: H. Yokpawa, S.C. Singhal (Eds.), Solid Oxide Fuel Cells (SOFC VII), The Electrochemical Society Proceedings Series, Pennington, New Jersey, 2001, PV2001-16, p. 895.
[12] C.M. Huang, S.S. Shy, C.H. Lee, ECS Trans. 7–2 (2007) 1849–1858 (oral presentation in SOFC-X, Nara, Japan, June 3–8, 2007).
[13] D. Lee, W.T. Hong, Y.N. Cheng, C.L. Huang, L.K. Chiang, M.S. Wang, Y.C. Tsai, R.Y. Lee, C.H. Lee, INER Research Report, INER-3636, 2005.
[14] CFD-RC, CFD-ACE$^+$ User Manual, Huntsville, USA, 2003, http://www.cfdrc.com.
[15] W. Lehnert, J. Meusinger, F. Thom, J. Power Sources 87 (2000) 57–63.
[16] K. Hou, R. Hughes, Chem. Eng. J. 82 (2001) 311–328.
[17] J.M. Klein, Y. Bultel, S. Georges, M. Pons, Chem. Eng. Sci. 62 (2007) 1636–1649.
[18] M. Cimenti, J.M. Hill, ECS Trans. 7–1 (2007) 1591–1600.
[19] Z.G. Yang, D.M. Paxton, K.S. Weil, J.W. Stevenson, P. Singh, PNNL Technical Report, PNNL-14116, 2002, pp. 64–73.